Publication Year	2018
Acceptance in OA	2020-10-14T14:18:09Z
Title	Protonated CO2 in massive star-forming clumps
Authors	FONTANI, FRANCESCO, Vagnoli, A., Padovani, Marco, Colzi, L., Caselli, P., RIVILLA RODRIGUEZ, VICTOR MANUEL
Publisher's version (DOI)	10.1093/mnrasl/sly160
Handle	http://hdl.handle.net/20.500.12386/27810
Journal	MONTHLY NOTICES OF THE ROYAL ASTRONOMICAL SOCIETY
Volume	481

MNRAS **000**, 1–?? (2017) Preprint 31 August 2018 Compiled using MNRAS LATEX style file v3.0

Protonated CO_2 in massive star-forming clumps

F. Fontani,[1]⋆ A. Vagnoli,[2] M. Padovani,[1] L. Colzi,[1,2] P. Caselli,[3] and V.M. Rivilla[1]
[1] *INAF-Osservatorio Astrofisico di Arcetri, Largo E. Fermi 5, I-50125, Florence, Italy*
[2] *Dipartimento di Fisica e Astronomia, Università degli Studi di Firenze, I-50125 Firenze, Italy*
[3] *Centre for Astrochemical Studies, Max-Planck-Institute for Extraterrestrial Physics, Giessenbachstrasse 1, 85748 Garching, Germany*

Accepted XXX. Received YYY; in original form ZZZ

ABSTRACT

Interstellar CO_2 is an important reservoir of carbon and oxygen, and one of the major constituents of the icy mantles of dust grains, but it is not observable directly in the cold gas because has no permanent dipole moment. Its protonated form, $HOCO^+$, is believed to be a good proxy for gaseous CO_2. However, it has been detected in only a few star-forming regions so far, so that its interstellar chemistry is not well understood. We present new detections of $HOCO^+$ lines in 11 high-mass star-forming clumps. Our observations increase by more than three times the number of detections in star-forming regions so far. We have derived beam-averaged abundances relative to H_2 in between 0.3 and 3.8×10^{-11}. We have compared these values with the abundances of $H^{13}CO^+$, a possible gas-phase precursor of $HOCO^+$, and CH_3OH, a product of surface chemistry. We have found a positive correlation with $H^{13}CO^+$, while with CH_3OH there is no correlation. We suggest that the gas-phase formation route starting from HCO^+ plays an important role in the formation of $HOCO^+$, perhaps more relevant than protonation of CO_2 (upon evaporation of this latter from icy dust mantles).

Key words: Stars: formation – ISM: clouds – ISM: molecules – Radio lines: ISM

1 INTRODUCTION

Carbon dioxide (CO_2) is a relevant molecular species in a variety of interstellar environments. In comets, planetary atmospheres, and interstellar ices, its abundance is a significant fraction ($\sim 0.1 - 0.5$) of that of water (e.g. Bergin et al. 2005, Whittet et al. 2009, McKay et al. 2016, Hoang et al. 2017). CO_2 ice is one of the main constituent of the icy mantles of dust grains (Öberg et al. 2011). In the gas-phase, CO_2 can be observed directly through ro-vibrational transitions (e.g. van Dishoeck et al. 1996), but the lack of permanent dipole moment, and hence of a pure rotational spectrum, makes it impossible a detection in cold environments. Instead, its protonated form, $HOCO^+$, has been detected towards the Galactic center (Thaddeus et al. 1981, Minh et al. 1991, Neill et al. 2014), in diffuse and translucent clouds (Turner et al. 1999), but only in a handful of star-forming regions: in the low-mass pre-stellar core L1544 (Vastel et al. 2016), in the protostars L1527 and IRAS 16293–2422 (Sakai et al. 2008, Majumdar et al. 2018), and in the protostellar shock L1157–B1 (Podio et al. 2014).

In cold and dense gas, two main chemical formation pathways have been proposed: **(1)** a gas-phase route from the reaction $HCO^+ + OH \leftrightarrow HOCO^+ + H$, and **(2)** the protonation of CO_2 (mainly upon reaction with H_3^+) desorbed from grain mantles (see e.g. Vastel et al. 2016, Bizzocchi et al. 2016). In scenario **(1)**, CO_2 would be a product of $HOCO^+$ (after dissociative recombination), while the opposite is expected in scenario **(2)**. Due to the lack of stringent observational constraints, it is unclear yet which of these two mechanisms is dominant, and under which physical conditions. Constraining the abundance of $HOCO^+$ has important implications also for the abundance of CO_2 in ice. In fact, if $HOCO^+$ is formed in the cold gas and then, upon dissociative recombination, gives rise to CO_2, this latter could freeze-out on grain mantles and contribute to the amount of CO_2 ice observed in dark clouds (Bergin et al. 2005), although this cannot explain the large amount of solid CO_2 measured along the line of sight of background stars (Boogert et al. 2015) or deeply embedded massive young stars (van Dishoeck et al. 1996). In fact, the formation of CO_2 ice from surface reactions is still debated. Laboratory experiments suggested formation of CO_2 ice from $CO + O \rightarrow CO_2$ (D'Hendecourt et al. 1986), which however needs a strong UV irradiation, and hence it is expected to be inefficient in dark clouds. Other surface reactions have been proposed, such as cosmic-ray bombardment on carbonaceous grains covered by water ice (Mennella et al. 2004), or the radical-radical reaction $OH + CO \rightarrow CO_2 + H$ (Garrod & Pauly 2011, Ioppolo et al. 2011, Noble et al. 2011). However, such process

---

⋆ E-mail: fontani@arcetri.astro.it

involves the diffusion of heavy radicals, difficult to happen at dust temperatures below ∼ 30 K, although high precision measurements are not available yet, and new promising techniques have been proposed (e.g. Cooke et al. 2016) to shed light on this important surface chemistry process.

In this paper, we present new detections of $HOCO^+$ in 11 high-mass star-forming regions, belonging to an evolutionary sample of 27 clumps divided into the three main evolutionary categories of the massive star formation process (Fontani et al. 2011): high-mass starless cores (HMSCs), high-mass protostellar objects (HMPOs) and Ultracompact HII regions (UCHIIs). The sample has been extensively observed in several dense gas tracers, with the aim of studying the chemical evolution of these molecules during the massive star-formation process (Fontani et al. 2011, 2014, 2015a, 2015b, 2016, Colzi et al. 2018a, 2018b, Mininni et al. 2018). This work represents the first study of protonated carbon dioxide in a statistically relevant number of star forming regions.

2 OBSERVATIONS

The spectra analysed in this work are part of the dataset presented in Colzi et al. (2018a). These data were obtained with the IRAM-30m Telescope in the 3 mm band with the EMIR receiver, covering the frequency ranges 85.31 – 87.13 GHz and 88.59 – 90.41 GHz, toward 26 dense cores in massive star-forming regions divided in the 3 evolutionary categories HMSCs, HMPOs and UCHIIs (see Sect. 1). For details on the source selection, see Fontani et al. (2011). The atmospheric conditions were very stable, with amounts of precipitable water vapour in the range 3 – 8 mm. We observed in wobbler-switching mode (wobbler throw of 240″). Pointing was checked almost every hour on nearby quasars, planets, or bright HII regions. The data were calibrated with the chopper wheel technique (see Kutner & Ulich 1981), and the calibration uncertainty is estimated to be about 10%. More details are given in Colzi et al. (2018a). The spectra have been reduced and analysed with the software CLASS of the GILDAS package. The detected lines have been fit with a gaussian shape.

3 RESULTS

Table 1 lists the 27 observed sources: 11 HMSCs, 9 HMPOs, and 7 UCHIIs. We have detected clearly (signal-to-noise ratio ≥ 5) the $HOCO^+$ $4_{0,4} - 3_{0,3}$ transition ($HOCO^+$ 4–3 hereafter, $E_{\rm up} \sim 10.3$ K) at 85531.497 MHz (Bizzocchi et al. 2016) in five HMSCs, two HMPOs and four UCHIIs. The spectra of the detected sources are shown in Fig. 1. The relatively high detection (∼ 50%) in the HMSCs indicates that $HOCO^+$ is a species abundant in cold and dense gas. The detection rate decreases during the HMPO phase (∼ 22%), and then it increases again at the UCHII stage (∼ 57%). Since we have detected only one transition of $HOCO^+$, to confirm that the detected line is indeed $HOCO^+$ and rule out contamination by transitions of other molecules, we have simulated the spectrum of one of the two sources in which the line has the highest intensity peak, namely 05358-mm1 (Fig. 1), and used the software MADCUBA[1] to search for emission of nearby lines potentially blended with $HOCO^+$ 4–3. Belloche et al. (2013) have shown that in Sgr B2(N) the only species with lines that could contaminate $HOCO^+$ 4–3 is C_2H_3CN. They found C_2H_3CN column densities above 10^{18} cm^{-2} and line widths larger than those that we have found for $HOCO^+$. To simulate the spectrum, we have assumed as excitation temperature the kinetic temperature obtained from ammonia (39 K, Fontani et al. 2011) and the same line width obtained fitting $HOCO^+$ 4–3 (4.9 km s^{-1}). As shown in Fig. 2 (top panel), even assuming a huge column density of 10^{18} cm^{-2} as in Sgr B2(N), the expected C_2H_3CN line intensities are well below the spectral rms, and well separate from the $HOCO^+$ 4–3 line. Another transition of $HOCO^+$, namely the $4_{1,3}$–$3_{1,2}$ line centred at 85852.8576 MHz ($E_{\rm u} \sim 48$ K), falls in our band but it is undetected. Because its line strength and Einstein coefficient are quite similar to those of the $4_{0,4} - 3_{0,3}$ transition (see Bizzocchi et al. 2016), we have investigated if its non-detection is due to the lack of sensitivity. Fig. 2 (bottom panel) shows that indeed the synthetic spectrum of 05358–mm1 around this line (simulated assuming the parameters described above for $HOCO^+$) is consistent with a non-detection. Because this source shows the highest intensity peak of $HOCO^+$ 4–3, we can reasonably conclude that the non-detection of the second transition is due to a sensitivity limit in all sources.

All detected lines are well fit by a single gaussian (Fig. 1). The results of the fit performed as explained in Sect. 2, namely line integrated intensity ($\int T_{\rm MB} {\rm d}v$), peak velocity in the Local Standard of Rest (LSR) ($v_{\rm p}$), and line width at half maximum (Δv) are shown in Table 1. The uncertainties on $\int T_{\rm MB} {\rm d}v$ are calculated from the expression $\sigma \Delta v_{\rm res} \sqrt{n}$, obtained from the propagation of errors, where σ is the 1σ root mean square noise in the spectrum, $\Delta v_{\rm res}$ the spectral resolution, and n the number of channels with signal. The uncertainties on $v_{\rm p}$ and Δv are computed by the fit procedure. The Δv measured towards the detected UCHII regions are always larger than ∼ 3.2 km s^{-1}, while they are narrower than 3 km s^{-1} in all HMSCs (but in 05358–mm3), in agreement with the fact that the envelopes of UCHII regions are more turbulent than those of HMSCs. The case of 05358–mm3 is peculiar because this core is likely externally heated (Fontani et al. 2011), hence its chemical composition and the emission that we observe is likely a mix between the cold and dense core nucleus and the warmer envelope. The line shapes are symmetric and do not show non-gaussian wings. This suggests that in all sources the $HOCO^+$ emission is associated with the bulk gas. This finding is supported by the fact that the peak velocities are consistent with the systemic velocities (given in Fontani et al. 2011) within the uncertainties (see Fig. 1).

3.1 $HOCO^+$ column densities and fractional abundances

From the line integrated intensity, we have calculated the total column density of $HOCO^+$ assuming Local Thermody-

---

[1] Madrid Data Cube Analysis on image is a software to visualize and analyse astronomical single spectra and datacubes (Martín et al., in prep., Rivilla et al. 2016).

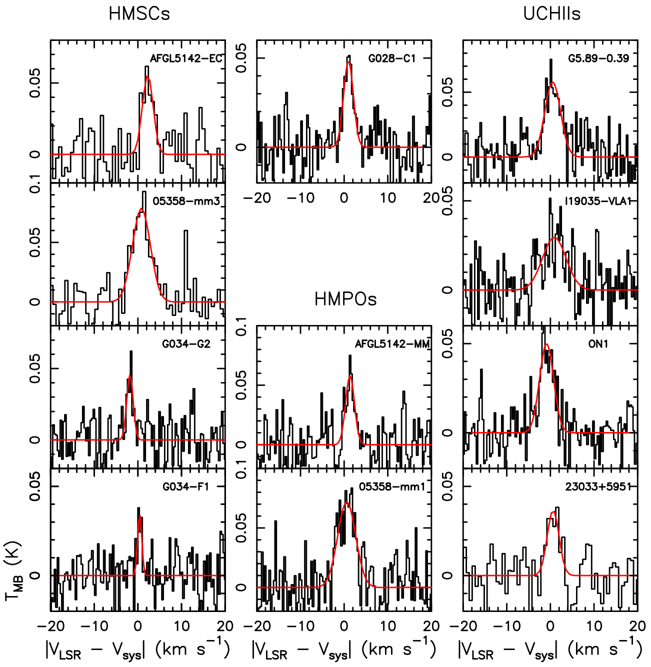

Figure 1. Spectra of the HOCO$^+$ ($4_{0,4} - 3_{0,3}$) line in the 11 detected sources. The y-axis is in $T_{\rm MB}$ units. The x-axis corresponds to $|V_{\rm LSR} - V_{\rm sys}|$, i.e. the difference between the local standard of rest velocity, $V_{\rm LSR}$, and the nominal systemic velocity, $V_{\rm sys}$, given in Fontani et al. 2011. The red curves superimposed on the spectra represent the best gaussian fits.

namic Equilibrium (LTE) and optically thin conditions from the equation:

$$N = \frac{8\pi\nu_{\rm ij}^3}{c^3 A_{\rm ij}} \frac{\int T_{\rm MB}{\rm d}v}{g_{\rm i}[J_\nu(T_{\rm ex}) - J_\nu(T_{\rm BG})]} \frac{Q(T_{\rm ex})\exp(E_{\rm j}/kT_{\rm ex})}{1-\exp(-{\rm h}\nu_{\rm ij}/{\rm k}T_{\rm ex})}, \qquad (1)$$

where $\nu_{\rm ij}$ is the frequency of the transition, $A_{\rm ij}$ is the Einstein coefficient of spontaneous emission, $g_{\rm i}$ is the statistical weight of the upper level, $E_{\rm j}$ is the energy of the lower level, c is the speed of light, h and k are the Planck and Boltzmann constants, respectively, $T_{\rm ex}$ is the excitation temperature, $Q(T_{\rm ex})$ is the partition function computed at temperature $T_{\rm ex}$, $T_{\rm BG}$ is the background temperature (assumed to be that of the cosmic microwave background, 2.7 K), and $J_\nu(T)$ is the equivalent Rayleigh-Jeans temperature (see also Eq. (A4) in Caselli et al. 2002). The line strength, energy of the upper level, and Einstein coefficient of spontaneous emission, are taken from the Cologne Database for Molecular Spectroscopy (CDMS[2], see also Bogey et al. 1986, and Bizzocchi et al. 2016), and are: $S\mu^2 \sim 29.2$ D^2, $E_{\rm u} \sim 10.3$ K, and $A_{\rm ij} \sim 2.36 \times 10^{-5}$ s^{-1}, respectively. The assumption of optically thin emission is consistent with the low abundance of the molecule and with line shapes without hints of high optical depths (like, e.g., asymmetric or flat topped profiles). The beam averaged column densities are in the range $\sim 3.5 \times 10^{11} - 4.6 \times 10^{12}$ cm^{-2}. For undetected lines, we have computed the upper limits on $\int T_{\rm MB}{\rm d}v$ assuming a gaussian line with intensity peak equal to the 3σ rms in the spectrum, and Δv equal to the average value of each evolutionary group, and from this we have derived the upper limits on N(HOCO$^+$) from Eq. 1.

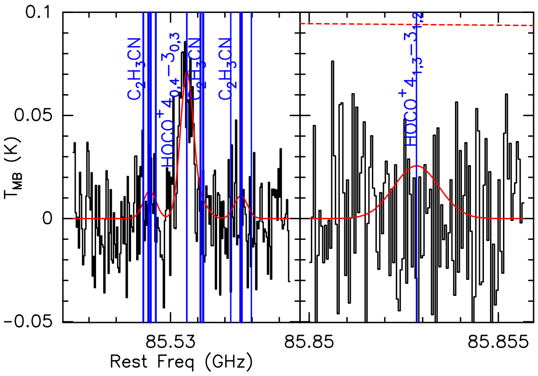

Figure 2. *Left panel*: spectrum of the HOCO$^+$ $4_{0,4} - 3_{0,3}$ line towards 05358–mm1 superimposed on the synthetic spectrum (in red) calculated with MADCUBA. The synthetic spectrum is calculated for a HOCO$^+$ column density of 4.3×10^{12} cm^{-2} and a C_2H_3CN column density of 10^{18} cm^{-2}, which is the value measured towards Sgr B2(N) (see Sect. 3). The rest frequencies of the nearby C_2H_3CN transitions are indicated by vertical lines. *Right panel*: spectrum of 05358–mm1 centred on the rest frequency of HOCO$^+$ $4_{1,3} - 3_{1,2}$, superimposed on the synthetic spectrum created with the same parameters used in Left panel: the expected peak of the line is well under the 3σ rms noise (shown by the red dashed horizontal line).

We have computed the HOCO$^+$ fractional abundances, X[HOCO$^+$], by dividing the HOCO$^+$ total column densities by those of H_2, $N(H_2)$, derived from the sub-millimeter continuum emission. This latter was computed from the (sub-)millimeter dust thermal continuum emission extracted from the images of the 850 μm survey of Di Francesco et al. (2008) obtained with SCUBA at the James Clerk Maxwell Telescope (JCMT). We have used Eq. (A1) in Mininni et al. (2018) to compute $N(H_2)$, which assumes optically thin emission, and a gas-to-dust ratio of 100. The sub-millimeter continuum fluxes, $F_{\rm submm}$, used to compute $N(H_2)$ have been extracted from a circular area equivalent to the IRAM-30m Half Power Beam Width (HPBW) at the frequency of the HOCO$^+$ line, i.e. $\sim 28''$. The uncertainty on $F_{\rm submm}$ is calculated from the propagation of errors. The sub-mm fluxes, and the derived $N(H_2)$ and X[HOCO$^+$] obtained as explained above, are given in Table 1. For the sources not present in the survey of Di Francesco et al. (2008), we have estimated $N(H_2)$ following the same analysis from the APEX ATLASGAL continuum images (http://www3.mpifr-bonn.mpg.de/div/atlasgal/index.html) at $\sim$ 870 GHz. We derive X[HOCO$^+$] in the range 0.3 – 3.8$\times 10^{-11}$. These values are intermediate between those obtained towards the pre-stellar core L1544 ($\sim 5 \times 10^{-11}$, Vastel et al. 2016) and the hot corino IRAS 16293–2422 ($\sim 1 \times 10^{-13}$, Majumdar et al. 2018).

4 DISCUSSION AND CONCLUSIONS

As discussed in Sect. 1, two main pathways have been proposed for the formation of HOCO$^+$ in dense gas: either the

---

[2] https://www.astro.uni-koeln.de/cdms

Table 1. Results derived from gaussian fits to the lines. In cols. 2–6 we give: integrated intensity ($\int T_{\rm MB}{\rm d}v$), velocity in the Local Standard of Rest (LSR) at line peak ($v_{\rm p}$), full width at half maximum (Δv), assumed gas excitation temperature ($T_{\rm ex}$), and HOCO$^+$ beam-averaged total column density, N(HOCO$^+$), calculated as explained in Sect. 3.1. The uncertainities on N are obtained propagating the error on $\int T_{\rm MB}{\rm d}v$, to which we sum a 10% of calibration error on the $T_{\rm MB}$ scale (see Sect. 2) not included in the error on $\int T_{\rm MB}{\rm d}v$. $T_{\rm ex}$ is assumed without uncertainty. Col. 7 and 8 give the sub-millimeter flux densities, $F_{\rm submm}$, and the H$_2$ column densities, N(H$_2$), derived from it, respectively (see Sect. 3.1 for details). The error on N(H$_2$) is obtained propagating the error on $F_{\rm submm}$, to which we add a calibration error of 20% on the SCUBA absolute flux scale at 850μm (Di Francesco et al. 2008). The HOCO$^+$ fractional abundances, X[HOCO$^+$], are shown in Col. 9. Finally, in Cols. 10, 11 and 12, we list the fractional abundances of CH$_3$OH, H^{13}CO$^+$, and N$_2$H$^+$ averaged over 28″.

Source	$\int T_{\rm MB}{\rm d}v$ K km s^{-1}	$v_{\rm p}$ km s^{-1}	Δv km s^{-1}	$T_{\rm ex}$ K	N(HOCO$^+$) $\times10^{11}$ cm^{-2}	$F_{\rm submm}$ Jy	N(H$_2$) $\times10^{22}$ cm^{-2}	X[HOCO$^+$] $\times10^{-11}$	X[CH$_3$OH] $\times10^{-10}$	X[H^{13}CO$^+$] $\times10^{-11}$	X[N$_2$H$^+$] $\times10^{-9}$
						HMSCs					
00117–MM2	≤ 0.069	–	–	14	≤ 3	–$^{(u)}$	–	–	–	–	–
AFGL5142–EC$^{(w)}$	0.17 ± 0.03	−1.6 ± 0.3	2.9 ± 0.6	25	9 ± 2	5.1±0.5$^{(s)}$	11.3±3.4	0.8±0.4	28±8	7.4±3.1	2.5±1.4
05358–mm3$^{(w)}$	0.41 ± 0.05	−16.8 ± 0.3	4.8 ± 0.6	30	23 ± 5	6.1±0.2$^{(s)}$	10.6±2.4	2.2±1.0	12±3	–	0.6±0.2
G034–G2	0.08 ± 0.02	41.8 ± 0.2	1.7 ± 0.5	20	4 ± 1	0.88±0.04$^{(a)}$	4.1±1.0	0.9±0.5	2.2±0.5	2.0±0.8	1.5±0.4
G034–F2	≤ 0.081	–	–	20	≤ 4	0.36±0.02$^{(s)}$	1.6±0.4	≤ 2.5	3.1±0.8	1.1±0.4	1.0±0.3
G034–F1	0.04 ± 0.01	58.1 ± 0.2	1.2 ± 0.4	20	1.9 ± 0.4	0.27±0.02$^{(s)}$	1.2±0.3	1.6±1.0	9.8±2.5	6.7±2.7	3.4±1.1
G028–C1	0.14 ± 0.02	79.3 ± 0.2	2.6 ± 0.4	17	6 ± 1	0.93±0.03$^{(s)}$	3.6±0.8	1.7±0.8	3.8±0.9	6±2	2.3±0.6
G028–C3	≤ 0.084	–	–	17	≤ 4	0.56±0.03$^{(a)}$	2.4±0.6	≤ 3.5	–	–	–
I20293–WC	≤ 0.074	–	–	17	≤ 3	1.9±0.1$^{(s)}$	7.4±1.9	≤ 0.4	2.4±0.6	4.9±1.9	1.5±0.5
22134–G$^{(w)}$	≤ 0.076	–	–	25	≤ 4	1.6±0.1$^{(s)}$	3.6±0.9	≤ 1.1	4±1	8.7±3.3	0.4±0.1
22134–B	≤ 0.071	–	–	17	≤ 3	0.52±0.05$^{(s)}$	2.0±0.6	≤ 1.6	0.9±0.3	4.8±2.0	0.9±0.4
						HMPOs					
00117–MM1	≤ 0.11	–	–	20	≤ 5	–$^{(u)}$	–	–	–	–	–
AFGL5142–MM	0.15 ± 0.03	−2.5 ± 0.2	2.4 ± 0.4	34	9 ± 3	6.8±0.3$^{(s)}$	10.1±2.4	0.9±0.5	53±13	10±4	2.4±0.7
05358–mm1	0.37 ± 0.04	−17.0 ± 0.2	4.9 ± 0.5	39	25 ± 5	6.1±0.3$^{(s)}$	8.4±2.1	3.0±1.4	30±8	1.0±0.4	1.4±0.04
18089–1732	≤ 0.13	–	–	38	≤ 8	7.5±0.4$^{(s)}$	9.6±2.4	≤ 0.8	67±17	14±5	2.2±0.8
18517+0437	≤ 0.12	–	–	40	≤ 8	6.7±0.4$^{(a)}$	7.9±1.3	≤ 1.0	54±9	21±6	1.1±0.2
G75–core	≤ 0.10	–	–	96	≤ 14	10.0±0.4$^{(s)}$	4.4±1.1	≤ 3.2	69±17	38±14	1.0±0.3
I20293–MM1	≤ 0.10	–	–	37	≤ 7	3.7±0.2$^{(s)}$	4.9±1.2	≤ 1.3	11±3	13±5	9±2
I21307	≤ 0.087	–	–	21	≤ 4	1.03±0.04$^{(s)}$	2.9±0.7	≤ 1.4	4.5±1.1	3.2±1.1	0.8±0.3
I23385	≤ 0.096	–	–	37	≤ 6	1.81±0.05$^{(s)}$	2.4±0.6	≤ 2.6	15±4	9.3±3.3	0.6±0.2
						UCHIIs					
G5.89–0.39	0.26 ± 0.03	9.5 ± 0.2	4.3 ± 0.6	31	15 ± 3	18±1$^{(s)}$	55±14	0.3±0.1	8.5±2	4.2±1.7	0.5±0.1
I19035–VLA1	0.20 ± 0.03	33.3 ± 0.4	6.4 ± 0.9	39	14 ± 3	2.9±0.1$^{(s)}$	3.6±0.9	3.8±1.9	17±4	15±5	5.0±1.5
19410+2336	≤ 0.15	–	–	21	≤ 7	4.8±0.1$^{(a)}$	13.6±3.0	≤ 0.5	5.4±1.2	3.6±1.2	3.2±1.0
ON1	0.20 ± 0.02	11.2 ± 0.2	3.8 ± 0.5	26	10 ± 2	–$^{(u)}$	–	–	–	–	–
I22134–VLA1	≤ 0.11	–	–	47	≤ 9	2.1±0.1$^{(s)}$	2.1±0.5	≤ 4.2	2.9±0.7	2.0±0.7	0.9±0.3
23033+5951	0.12 ± 0.02	−52.4 ± 0.3	3.2 ± 0.5	25	7 ± 2	3.5±0.1$^{(s)}$	7.8±1.8	0.8±0.4	5.7±1.3	9.2±3.1	2.6±1.4
NGC7538–IRS9	≤ 0.16	–	–	31	≤ 10	3.9±0.1$^{(s)}$	11.9±2.7	≤ 0.8	5.4±1.2	4.1±1.4	0.5±0.1

$^{(w)}$ "warm" core having a kinetic temperature higher than 20 K, and likely externally heated (Fontani et al. 2011); $^{(s)}$ measured from the maps of the SCUBA survey (Di Francesco et al. 2008); $^{(a)}$ measured from the maps of the APEX ATLASGAL survey (http://www3.mpifr-bonn.mpg.de/div/atlasgal/index.html); $^{(u)}$ continuum map not available either in the survey of Di Francesco et al. (2008) or in the ATLASGAL survey.

gas-phase reaction HCO$^+$ + OH ↔ HOCO$^+$ + H, or the protonation of desorbed CO$_2$, mainly upon reaction with H$_3^+$ (Vastel et al. 2016, Bizzocchi et al. 2016). To investigate if and how our observational results can put constraints on these alternative pathways, in Fig. 3 we show the fractional abundance of HOCO$^+$ (calculated as explained in Sect. 3.1) against that of H^{13}CO$^+$, the main precusor of HOCO$^+$ in the gas phase, and CH$_3$OH, a tracer of surface chemistry. For completeness, we also plot X[HOCO$^+$] against X[N$_2$H$^+$], because protonation of CO$_2$ may occur also via reaction with N$_2$H$^+$. The CH$_3$OH and N$_2$H$^+$ column densities used to compute X[CH$_3$OH] and X[N$_2$H$^+$] have been taken from Fontani et al. (2015a) and Fontani et al. (2015b), respectively, and rescaled to the beam of the HOCO$^+$ observations.

The H^{13}CO$^+$ column densities used to derive X[H^{13}CO$^+$] have been estimated from the integrated intensities of the H^{13}CO$^+$ 1–0 lines at 86754.288 MHz, serendipitously detected in the same dataset described in Sect. 2 and in Colzi et al. (2018a). We have followed the same approach used for HOCO$^+$, namely we assumed optically thin lines and LTE conditions (see Sect. 3.1). We used the excitation temperatures listed in Table 1. The beam size is almost the same of that of HOCO$^+$, hence all the fractional abundances in Table 1 are averaged over the same angular region.

Figure 3 indicates a clear non-correlation between the abundances of CH$_3$OH and HOCO$^+$, while H^{13}CO$^+$ and HOCO$^+$ seems positively correlated. By applying simple statistical tests to the detected sources only, the correlation co-

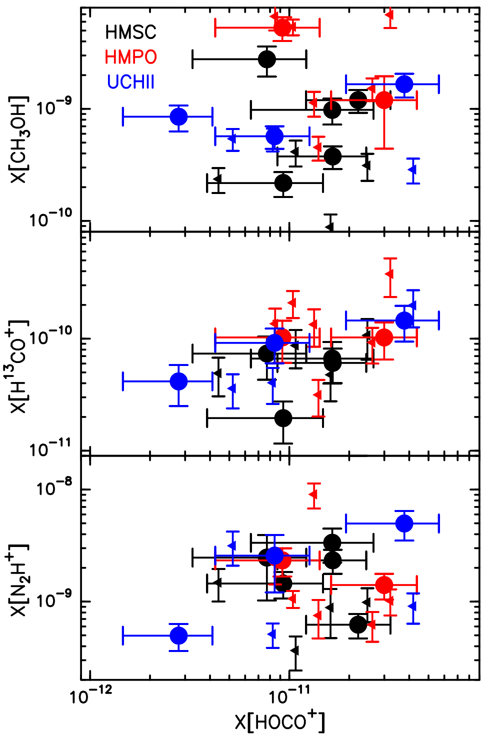

Figure 3. Abundance of $HOCO^+$ against that of, from top to bottom: CH_3OH, $H^{13}CO^+$, and N_2H^+. The colours indicate the different evolutionary groups as labelled in the top-left corner. The large filled symbols correspond to the detected sources, while the small triangles indicate the upper limits on the abundance of $HOCO^+$. In the panel with X[$H^{13}CO^+$], we do not show 05358-mm3, observed and detected in CH_3OH, N_2H^+ and $HOCO^+$ but not in $H^{13}CO^+$.

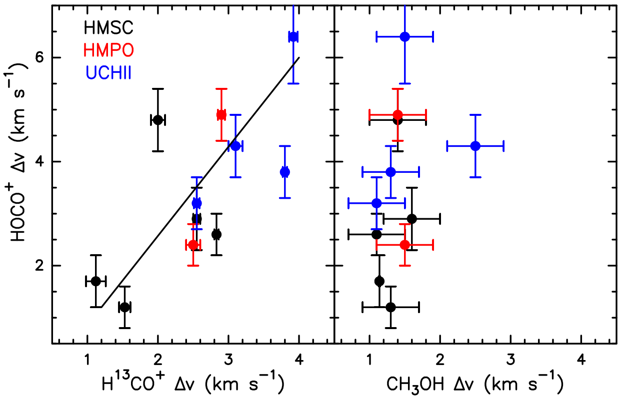

Figure 4. Line widths at half maximum, Δv, of $H^{13}CO^+$ (left panel) and CH_3OH (right panel) against those of $HOCO^+$. The colours indicate the different evolutionary groups as in Fig. 3. The solid line in the left panel corresponds to a linear fit to the data.

efficient (Pearson's ρ) between X[$HOCO^+$] and X[$H^{13}CO^+$] is 0.7. Considering also the upper limits, the correlation remains positive (Pearson's $\rho = 0.6$). The correlation between X[$HOCO^+$] and X[N_2H^+] is positive (Pearson's $\rho = 0.4$ without the upper limits) but much less convincing. If we assume that both CO_2 and CH_3OH form on grain mantles, and what we find in the gas is evaporated at similar times, the lack of correlation between X[$HOCO^+$] and both X[CH_3OH] and X[N_2H^+] would indicate that the origin of $HOCO^+$ is likely not from CO_2 evaporated from ice mantles. This interpretation has two big caveats. First, the formation processes of CO_2 and CH_3OH on the surfaces of dust grains can be different. In fact, CO_2 is thought to form in water ice mantles of cold carbonaceous grains via cosmic-ray bombardment (Mennella et al. 2004), or via the surface reaction CO + OH at dust temperatures of ~30 K (Garrod & Pauly 2011), while CH_3OH if formed from hydrogenation of CO at dust temperatures ~ 10 K (Vasyunin et al. 2017). Second, the main molecular ion responsible for the protonation of CO_2 is H_3^+ and not N_2H^+. Nevertheless, the positive correlation between X[$H^{13}CO^+$] and X[$HOCO^+$] suggests a non negligible, or even dominant, contribution from HCO^+ to the formation of the detected $HOCO^+$. This interpretation of our results is in agreement with the study of Majumdar et al. (2018), who proposed that the dominant (up to 85%) formation route of $HOCO^+$ in the extended and cold ($T \leq 30$ K) envelope of the hot corino IRAS 16293–2422 is indeed from the gas-phase reaction OH + HCO^+. The fact that $HOCO^+$ and $H^{13}CO^+$ likely arise from similar gas can be understood also from the comparison of their line widths at half maximum. Fig. 4 indicates that the $HOCO^+$ line widths are correlated with those of $H^{13}CO^+$, but not with those of CH_3OH (which are always narrower). Hence, CH_3OH is likely not associated with the same gas.

Overall, our findings suggest a significant (perhaps dominant) role of HCO^+ as a gas-phase progenitor of $HOCO^+$. However, caution needs to be taken in the interpretation of our results for several reasons. First, the $HOCO^+$ column densities, and hence the fractional abundances, have been derived assuming an excitation temperature that could not be that of the molecule. To solve this problem, detection of more lines tracing different excitation conditions are absolutely required. Another caveat arises from the fact that our column densities are values averaged over large (28″) angular surfaces. Our targets are known to have complex structure, and temperature (and density) gradients. Therefore, higher angular resolution observations are needed to precisely determine the $HOCO^+$ emitting region, and, from this, understand its temperatures and densities, required to properly model the chemistry.

Acknowledgments. We thank the IRAM-30m staff for the precious help during the observations. We thank the anonymous referee for his/her constructive comments. V.M.R. and M.P. acknowledge the financial support received from the European Union's Horizon 2020 research and innovation programme under the Marie Sklodowska-Curie grant agreement No 664931. L.C. acknowledges support from the Italian Ministero dell'Istruzione, Università e Ricerca through the grant Progetti Premiali 2012 - iALMA (CUP C52I13000140001). P.C. acknowledges support from the European Research Council (ERC project PALs 320620).

REFERENCES

Belloche, A., Müller, H.S.P., Menten, K.M., Schilke, P., Comito, C. 2013, A&A, 559, 47

Bergin, E.A., Melnick, G.J., Gerakines, P.A., Neufeld, D.A., Whittet, D.C.B. 2005, ApJ, 627, L33

Bizzocchi, L., Lattanzi, V., Laas, J., Spezzano, S., Giuliano, B.M., Prudenzano, D., Endres, C. et al. 2017, A&A, 602, 34

Bogey, M., Demuynck, C., Destombes, J.-L. 1986, JChPh, 84, 10

Boogert, A.C.A., Gerakines, P.A., Whittet, D.C.B. 2015, ARA&A, 53, 541

Caselli, P., Walmsley, C.M., Zucconi, A., et al. 2002, ApJ, 565, 344

Colzi, L., Fontani, F., Caselli, P., Ceccarelli, C., Hily-Blant, P., Bizzocchi, L. 2018a, A&A, 609, 129

Colzi, L., Fontani, F., Rivilla, V.M., Sánchez-Monge, A., Testi, L., Beltrán, M.T., Caselli, P. 2018b, MNRAS, 478, 3693

Cooke, I.R., Fayolle, E.C., Öberg, K.I. 2016, ApJ, 832, 5

D'Hendecourt, L.B., Allamandola, L.J., Grim, R.J.A., Greenberg, J.M. 1986, A&A, 158, 119

Di Francesco, J., Johnstone, D. Kirk, H., MacKenzie, T., Ledwosinska, E. 2008, ApJS, 175, 277

Fontani, F., Palau, A., Caselli, P., Sánchez-Monge, Á., Butler, M. J. 2011, A&A, 529, L7

Fontani, F., Sakai, T., Furuya, K., Sakai, N., Aikawa, Y., Yamamoto, S. 2014, MNRAS, 440, 448

Fontani, F., Busquet, G., Palau, Aina, Caselli, P., Sánchez-Monge, Á., Tan, J.C., Audard, M. 2015a, A&A, 575, 87

Fontani, F., Caselli, P., Palau, A., Bizzocchi, L., Ceccarelli, C. 2015b, ApJ, 808, L46

Fontani, F., Rivilla, V.M., Caselli, P., Vasyunin, A., Palau, A. 2016, ApJ, 822, L30

Garrod, R.T & Pauly, T. 2011, ApJ, 735, 15

Hoang, M., Altwegg, K., Balsiger, H., Beth, A., Bieler, A. et al. 2017, A&A, 600, 77

Ioppolo, S., van Boheemen, Y., Cuppen, H.M., van Dishoeck, E.F., Linnartz, H. 2011, MNRAS, 413, 2281

Kutner, M.L. & Ulich, B.L. 1981, ApJ, 250, 341

Majumdar, L., Gratier, P., Wakelam, V., Caux, E., Willacy, K., Ressler, M.E. 2018, MNRAS, 477, 525

McKay, A.J., Kelley, M.S.P., Cochran, A.L., Bodewits, D., DiSanti, M.A., Russo, N.D., Lisse, C.M. 2016, Icarus, 266, 249

Mennella, V., Palumbo, M.E., Baratta, G.A. 2004, ApJ, 615, 1073

Minh, Y.C., Brewer, M.K., Irvine, W.M., Friberg, P., Johansson, L.E.B. 1991, A&A, 244, 470

Mininni, C., Fontani, F., Rivilla, V.M., Beltrán, M.T., Caselli, P., Vasyunin, A. 2018, arXiv:180200623

Neill, J. L., Bergin, E. A., Lis, D. C., et al. 2014, ApJ, 789, 8

Noble, J.A., Dulieu, F., Congiu, E., Fraser, H.J. 2011, ApJ, 735, 121

Öberg, K.I., Boogert, A.C.A., Pontoppidan, K.M., van den Broek, S., van Dishoeck, E.F., et al. 2011, ApJ, 740, 109

Podio, L., Lefloch, B., Ceccarelli, C., Codella, C., Bachiller, R. 2014, A&A, 565, 64

Rivilla, V.M., Fontani, F., Beltrán, M.T., Vasyunin, A., Caselli, P., Martín-Pintado, J., Cesaroni, R. 2016, ApJ, 826, 161

Sakai, N., Sakai, T., Aikawa, Y., Yamamoto, S. 2008, ApJ, 675, L89

Thaddeus, P., Guelin, M., & Linke, R. A. 1981, ApJ, 246, L41

Turner, B. E., Terzieva, R., & Herbst, E. 1999, ApJ, 518, 699

van Dishoeck, E.F., Helmich, F.P., de Graauw, T., Black, J.H., Boogert, A.C.A., et al. 1996, A&A, 315, L349

Vastel, C., Ceccarelli, C., Lefloch, B., Bachiller, R. 2016, A&A, 591, L2

Vasyunin, A.I., Caselli, P., Dulieu, F., Jiménez-Serra, I. 2017, ApJ, 842, 33

Whittet, D.C.B., Cook, A.M., Chiar, J.E., Pendleton, Y.J., Shenoy, S.S., Gerakines, P. A. 2009, ApJ, 695, 94